Generalized Noh self-similar solutions of the compressible Euler equations for hydrocode verification

A.L. Velikovich [a,*], J.L. Giuliani [a], S.T. Zalesak [b]

[a] *Plasma Physics Division, Naval Research Laboratory, Washington, DC 20375, USA*
[b] *KeyW Corporation, Hanover, MD 21076, USA*

A B S T R A C T

A family of exact self-similar solutions of the compressible Euler equations developed for hydrocode verification is described. This family generalizes the classic Noh problem, which has served as a standard verification test of numerical methods for modeling inviscid compressible flows for three decades. This generalization allows finite pressure initial conditions, nearly arbitrary equations of state, and describes shocked compression as well as isentropic expansion and compression of the gas. In particular, the solutions describe a) the propagation of a finite-strength spherical isentropic expansion wave into a moving uniform gas, leaving behind either a core of uniform gas at rest or a vacuum/cavitation; b) the convergence of a finite-strength isentropic compression wave into a uniform gas or a collapse of a cavity in a finite-pressure gas (a compressible analog of the Rayleigh problem); and c) the expansion of a finite-strength accretion shock wave into a converging isentropic flow of stagnating gas. Our proposed verification test seeks to numerically reproduce all three of these stages of gas motion in a single simulation run. The successful verification of a high-order Godunov Eulerian hydrodynamics code is presented as an example of the expected use of this family of exact solutions.

Published by Elsevier Inc. This is an open access article under the CC BY license
(http://creativecommons.org/licenses/by/4.0/).

1. Introduction

The method of exact solutions [1], which compares simulation results with the known solution of an idealized problem, remains a valuable tool of code verification. In one-dimensional compressible gas dynamics, there are a number of problems that permit exact solutions suitable for code verification. The simplest of them is the planar Riemann problem, the evolution of a step-function discontinuity in the initial conditions. For polytropic gases, its solution, first obtained by Kochin [2], is described in detail in [3], §100. (In the literature on code verification, one particularly popular Riemann problem is the Sod shock-tube problem [4,5].) Exact self-similar solutions of Riemann problems involve constant-intensity shock waves and/or centered rarefaction waves and/or a material interface or a tangential discontinuity. For a planar geometry, these solutions provide good verification tests.

For spherical and cylindrical geometries, the simplest verification test is provided by the Noh problem [6]: an initially uniform gas at zero pressure stagnates against a plane, axis, or center of symmetry. (For a planar geometry, the Noh problem obviously reduces to a particular case of a Riemann problem.) Its self-similar solutions contain an expanding accretion shock front that propagates at a constant velocity into a non-uniform flow of a converging zero-pressure gas. These solutions

---

* Corresponding author.
E-mail address: sasha.velikovich@nrl.navy.mil (A.L. Velikovich).

have been used for three decades to verify codes designed to model implosion and stagnation. Their main advantage is, as described in [7], "the simplicity of the initial and final conditions in three geometries": all the flow variables have uniform profiles initially, and they remain finite at all times. Moreover, their self-similar profiles are given by explicit analytic formulas. None of the other classic self-similar solutions of the compressible Euler equations, such as Sedov–Taylor–von Neumann blast wave [8,9] or Guderley shock-wave implosion [10], have all these advantages, which makes their use for code verification much more difficult, though not impossible [11,12].

Notwithstanding the apparent simplicity of the Noh problem formulation and numerical initialization, this benchmarking test "poses a formidable challenge to all hydrodynamics codes since they have to deal with an infinitely strong shock" [7], and is able "to dramatically reflect any underlying numerical solver pathologies (e.g., asymmetries and wall-heating phenomena)" [13].

As correctly observed in Ref. [1], the main disadvantage of the method of exact solutions for code verification is that "there are only a limited number of exact solutions available for complex equations (i.e., those with complex geometries, physics, or nonlinearity)." To help address this dearth of exact verification tests, a number of authors have developed new exact solutions of the compressible Euler equations that account for more physics and include complex geometries. In particular, the original Noh solution, henceforth referred to as "classic," has been recently generalized in various ways. A piston/shock tube problem involving multiple shock reflections from the piston and the plane/center/axis of symmetry has been studied in Ref. [7]. The Noh problem for a non-ideal equation of state (EOS), such as Mie–Grüneisen, has been solved in Refs. [13,14]. Generalized solutions of the Noh problem for non-uniform velocity, density and pressure profiles are presented in Ref. [15]. A magnetohydrodynamic (MHD) modification of the Noh problem for a Z-pinch geometry of magnetic field is given in Ref. [16]. A linear perturbation analysis of the classic Noh solutions [17] made it possible to benchmark two- and three-dimensional codes describing the evolution of small perturbations on top of an unsteady stagnation flow in cylindrical and spherical geometry, respectively.

Here, we derive another generalization of the classic Noh solution. We remove the zero-initial-pressure constraint, finding solutions that describe finite-strength shocks. Reproducing such solutions numerically might be less of a "formidable challenge" [7] for code verification than the classic Noh solution, since zero initial pressure can not only be problematic for hydrocodes, but can cause difficulty even for particle-in-cell or kinetic codes when used to model hydrodynamic plasma flows (see, for example, Refs. [18] and [19]), and such codes would also benefit greatly from verification tests. Self-similar solutions of this family include: 1) spherical and cylindrical rarefaction waves analogous to the centered rarefaction waves that can appear in planar Riemann problems; 2) isentropic finite-strength compression waves that steepen as they propagate to eventually form shock waves; 3) both the convergence/implosion phase and the stagnation/expansion phase described by the same solution, similar to the case of the Guderley problem [10,11]. There is also another similarity with the Guderley problem: our new solutions are not given by explicit formulas, they are evaluated using numerical integration of the ordinary differential equations determining the self-similar profiles. As far as code verification is concerned, such semi-analytic solutions are considered "exact" [11] because their numerical accuracy is typically higher than that of the hydrocodes they are used to verify.

Our new solutions are presented for a polytropic ideal gas. They could be further generalized for an ideal fluid with an arbitrary EOS, which does not have to satisfy the Lie symmetry constraints outlined in [9,13,14], and for MHD in a cylindrical Θ-pinch geometry. Both the solutions described here and their possible generalizations permit linear perturbation analysis [17] resulting in explicit analytical dispersion equations. Thus these solutions can be used to generate verification tests for compressible gasdynamic and MHD codes in two and three dimensions, by testing not only the ability of such codes to reproduce the analytic unperturbed one-dimensional solution, but also to reproduce the proper behavior of small-amplitude perturbations applied to that solution in the transverse directions.

This paper is structured as follows. In Section 2, we present a derivation of the new self-similar solutions of the compressible Euler equations. In Section 3, we compare our semi-analytic solutions to the numerical solutions produced by a particular one-dimensional, high-order Godunov Eulerian code, in order to demonstrate how these solutions can be used for hydrocode verification. In Section 4, we conclude with a discussion.

2. Theory

2.1. Formulation of the Noh problem and governing equations

The Noh problem formulation is illustrated with Fig. 1, the terminology and sub-figures of which we refer to extensively in this and the following two paragraphs. Fig. 1(a) schematically shows the initial conditions at $t = 0^-$: uniform gas density ρ_0, pressure p_0, and velocity v_0 directed to the center of symmetry everywhere but at $r = 0$. These initial conditions produce an accretion shock front expanding at a constant velocity v_s at $t > 0$, Figs. 1(b) and (c). The gas behind the shock front is labeled "Uniform shocked gas at rest." The shock front expands into the stagnating incident gas flow whose spherical convergence increases the gas density in the negative radial direction. If the initial gas pressure $p_0 = 0$, then the adiabatic gas compression does not lead to a pressure increase. Hence, the pre-shock gas velocity also stays the same, $-v_0$, as shown in Fig. 1(b), which corresponds to the classic Noh solution. On the other hand, if $p_0 > 0$, then the gas compression leads to an adiabatic pressure increase in the negative radial direction, which, in turn, slows down the converging pre-shock gas, as schematically shown in Fig. 1(c). This situation corresponds to a generalized accretion-shock Noh solution.
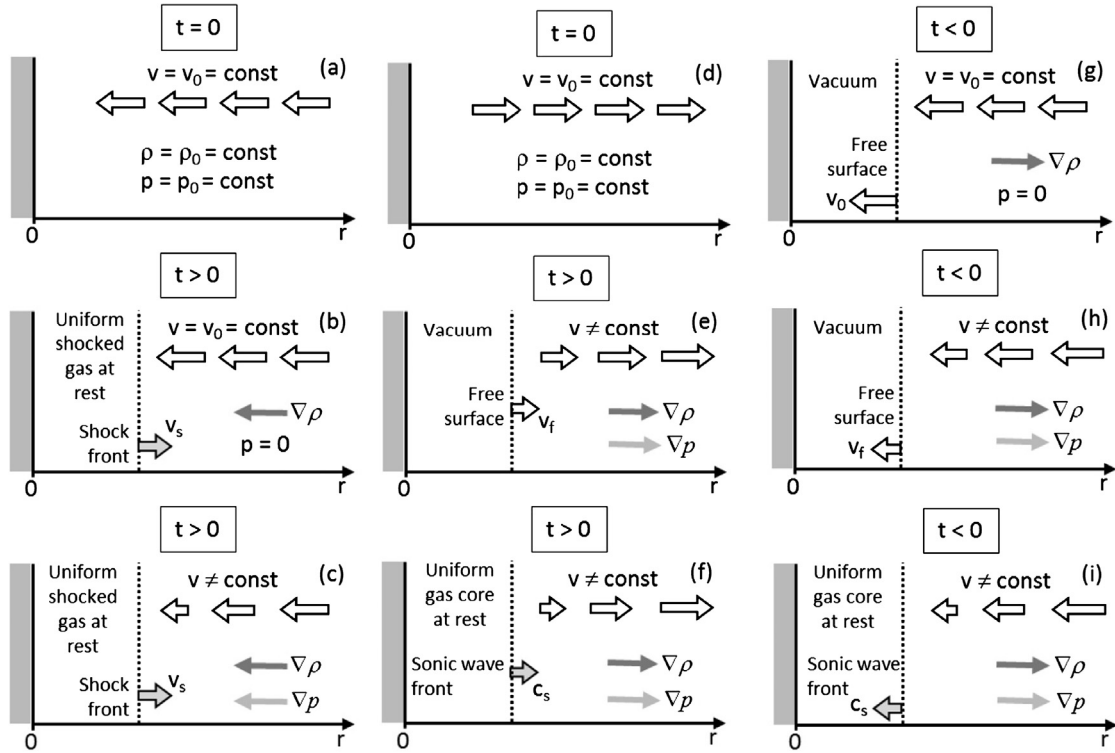
Fig. 1. Schematic of the generalized Noh flows. (a) Converging-flow initial conditions at $t = 0^-$. (b) Stagnation phase for a cold imploding gas, $p_0 = 0$. (c) Stagnation phase for a finite-pressure imploding gas, $p_0 > 0$. (d) Diverging-flow initial conditions at $t = 0^-$. (e) Rarefaction wave in a finite-pressure gas, $p_0 > 0$, leaving a vacuum behind. (f) Rarefaction wave in a finite-pressure gas leaving a uniform gas core at rest behind. (g) Collapse of a cavity in a cold gas. (h) Collapse of a cavity in a finite-pressure gas. (i) Convergence of a finite-strength compression wave onto a uniform gas core at rest.

If the velocity v_0 at $t = 0^-$ is directed from the center of symmetry everywhere but at $r = 0$, as shown in Fig. 1(d), then a spherically expanding rarefaction wave will emerge at $t > 0$. When the expansion velocity v_0 is sufficiently large compared to the initial speed of sound, then the rarefaction wave leaves behind an empty cavity labeled "Vacuum" in Fig. 1(e). Its outer boundary, where the gas density and pressure both vanish, is labeled "Free surface." The velocity profile is non-uniform, the velocity of the free surface denoted v_f being the lowest radial velocity directed outward. When the velocity v_0 is not large enough, the rarefaction wave leaves behind a "Uniform gas core at rest," as shown in Fig. 1(f). It is bounded by the trailing edge of the expanding rarefaction wave, a weak discontinuity labeled "Sonic wave front" that propagates at the speed of sound c_s characteristic of the uniform gas core.

Being isentropic, the solutions illustrated with Figs. 1(e), (f) are reversible. It means that the same solutions considered at negative time, from $t = -\infty$ to $t = 0^-$, describe the collapse of a cavity in a cold gas, Fig. 1(g), or in a finite-pressure gas, Fig. 1(h), or a spherical convergence of a finite-strength compression wave, Fig. 1(i). The cavity collapse cases are compressible analogs of the well-known Rayleigh problem, the collapse of a bubble in an incompressible fluid, described in Chapter XII, Section 9 of Ref. [20]. In all cases, the steepening of density and pressure profiles due to the spherical convergence results in the formation of the uniform profiles shown in Fig. 1(a) at the instant of collapse when the wave front reaches the center, $t = 0^-$. When the collapsing gas is cold, Fig. 1(g), then the velocity of all gas particles, including those at the free surface, equals $-v_0$ at all time, and the gas pressure remains zero up to the moment of collapse. This case can be regarded as the classic Noh flow at $t < 0$, prior to the instant illustrated with Fig. 1(a). In the other two cases, the gas velocity profiles during the convergence stage are non-uniform, as shown in Figs. 1(h), (i), the velocity of the free surface v_f being the lowest radial velocity directed inward. The uniform pressure p_0 produced at the instant of collapse, $t = 0^-$, is positive. These cases can be regarded as generalized Noh flows at the negative time.

We seek self-similar solutions that describe the flows schematically shown in Figs. 1(b), (c), (e)–(i). For this purpose, we solve the ideal gas dynamic equations for a spherical geometry:

$$\frac{\partial \ln \rho}{\partial t} + v \frac{\partial \ln \rho}{\partial r} + \frac{\partial v}{\partial r} + \frac{2v}{r} = 0, \tag{1}$$

$$\frac{\partial \ln p}{\partial t} + v \frac{\partial \ln p}{\partial r} + \gamma \frac{\partial v}{\partial r} + 2\gamma \frac{v}{r} = 0, \tag{2}$$

$$\frac{\partial v}{\partial t} + v \frac{\partial v}{\partial r} + \frac{1}{\rho} \frac{\partial p}{\partial r} = 0. \tag{3}$$

The case of cylindrical geometry is described by the same equations with the geometric factor 2 in Eqs. (1), (2) replaced with unity. It is studied in exactly the same way as the case of spherical geometry, and we are not addressing it here.

The problem under consideration is defined by the initial conditions imposed at $t = 0^-$:

$$v(r, t = 0^-) = \begin{cases} 0, & r = 0; \\ \pm v_0, & r > 0, \end{cases} \tag{4}$$

$$\rho(r, t = 0^-) = \rho_0, \tag{5}$$

$$p(r, t = 0^-) = p_0, \tag{6}$$

where the constant $v_0 > 0$ is the absolute value of the initial uniform expansion or compression velocity; the constants $\rho_0 > 0$ and $p_0 \geq 0$ are the initial values of the density and pressure. The initial conditions (4)–(6) for the negative and positive signs in front of v_0 in (4) correspond to the cases illustrated with Figs. 1(a) and (d), respectively. The boundary conditions are

$$v(r = 0, t > 0) = \begin{cases} 0, & \text{if } \rho(r = 0, t) > 0, \\ \text{undefined otherwise;} \end{cases} \tag{7}$$

$$v(r \to \infty, t > 0) = \pm v_0, \qquad \rho(r \to \infty, t > 0) = \rho_0, \qquad p(r \to \infty, t > 0) = p_0.$$

The single dimensionless parameter determining the problem for a given value of gas γ and a specified geometry is the Mach number

$$M_0 = \frac{v_0}{c_{s0}} = \frac{v_0}{\sqrt{\gamma p_0 / \rho_0}}. \tag{8}$$

To find the self-similar solutions sought for, we use the symmetry of our initial/boundary value problem (1)–(7). Our governing equations (1)–(3), as well as the initial and boundary conditions (4)–(7), are invariant under the Abelian group of scale (or dilatation) transformations of radius and time

$$r \to \lambda r, \qquad t \to \lambda t, \tag{9}$$

which leave the velocity, density, and pressure unchanged. Here, the scale factor λ is an arbitrary positive number. Therefore, as explained in many physical and mathematical texts (see, for example, Chapter XII, Section 2 of Ref. [20] and Chapter V, Section 19 of Ref. [21]), solutions of our problem are self-similar, depending on the independent variables r and t only via their dimensionless combination, which in our case is $r/(v_s t)$.

Other relevant symmetries of Eqs. (1)–(7) involve transformations of the initial and boundary conditions. For example, the simultaneous inversion of time and velocity,

$$t \to -t, \qquad v \to -v, \tag{10}$$

which leaves Eqs. (1)–(3), the radius, density, and pressure unchanged, changes the sign in front of v_0 in (4) and (7), and makes the boundary conditions (7) formulated for the negative time, $t < 0$. This symmetry transforms the rarefaction-wave solutions illustrated with Figs. 1(e) and (f) into the collapsing-cavity and the converging-compression-wave solutions illustrated with Figs. 1(h) and (i), respectively. Note that the symmetry transformation (10) cannot be applied to the generalized Noh solutions that involve accretion shocks, Figs. 1(b), (c). Shock fronts generate entropy, and non-isentropic flows are not reversible.

Similarly, the time translations

$$t \to t - t_0, \tag{11}$$

where t_0 is an arbitrary value, do not affect Eqs. (1)–(3) but require appropriate modifications of the initial and boundary conditions (4)–(7). In Fig. 1, this corresponds to replacing $t = 0$, $t > 0$ and $t < 0$ with $t = t_0$, $t > t_0$ and $t < t_0$, respectively. In particular, for converging-shell and converging-compression-wave flows illustrated with Figs. 1(h), (i), the instant of collapse after this transformation will be t_0^-.

2.2. Self-similarity ansatz

Here we describe in detail the family of the self-similar solutions whose existence had been first noted in [9], Chapter 4, Section 7 titled "The problem of an implosion and explosion at a point." Later, solutions of this family were discussed in [22] in the context of magnetized target fusion research, as examples of exact solutions that describe both implosion and stagnation of a plasma shell, where "the post-stagnation hot core plasma does not expand against the imploding flow."

We introduce the self-similar variables in the usual way, as done, for example, in [8–11,13–17,20,22–28]. The self-similar radial coordinate is defined as

$$\eta = \frac{r}{v_s |t|} \geq 0. \tag{12}$$

The negative time $t < 0$ corresponds to the implosion phase of the flow, when its radial length scale $v_s|t|$ decreases with time to vanish at $t = 0$. The positive time $t > 0$ corresponds to the stagnation phase of the flow, when its radial length scale, which coincides with the accretion shock radius, increases linearly with time, while the pre-shock gas keeps converging to the center. The dimensional velocity, density, and pressure are expressed as

$$v(r, t) = v_s \, \mathrm{sgn}(t) \eta U(\eta), \tag{13}$$

$$\rho(r, t) = \rho_0 N(\eta), \tag{14}$$

$$p(r, t) = \rho_0 v_s^2 P(\eta), \tag{15}$$

where $U(\eta)$, $N(\eta)$, and $P(\eta)$ are dimensionless functions determining the self-similar profiles. According to our definitions (12), (13), at $t > 0$, positive and negative values of $U(\eta)$ correspond to radially diverging and converging flows, whereas at $t < 0$ it is the other way around. Passing into the self-similar variables (13)–(15), we transform Eqs. (1)–(3) into the ordinary differential equations:

$$(U - 1)\frac{d \ln N}{d \ln \eta} + \frac{dU}{d \ln \eta} + 3U = 0, \tag{16}$$

$$(U - 1)\frac{d \ln P}{d \ln \eta} + \gamma \frac{dU}{d \ln \eta} + 3\gamma U = 0, \tag{17}$$

$$(U - 1)\left(\frac{dU}{d \ln \eta} + U\right) + \frac{P}{\eta^2 N}\frac{d \ln P}{d \ln \eta} = 0. \tag{18}$$

We introduce a new self-similar variable

$$S = \frac{\gamma P}{\eta^2 N (1 - U)}. \tag{19}$$

Most other authors use instead one of the equivalent variables, like $Z = S(1 - U)$ or $C = \sqrt{Z}$ [3,8–11,20,22–26]. Our choice of the sonic variable S was determined specifically by its convenience for the MHD generalization, see [16,27,28]. Obviously, the variables $P(\eta)$ and $N(\eta)$ cannot be negative, so the physically meaningful domains of variation of $U(\eta)$ and $S(\eta)$ are ($U \leq 1, S \geq 0$) and ($U \geq 1, S \leq 0$). In the context of the problem under consideration, only the former domain is of interest, see Section 2.3 below.

With the aid of Eqs. (16), (17), we immediately obtain an equation for $S(\eta)$:

$$(U - 1)\frac{d \ln S}{d \ln \eta} + \gamma \frac{dU}{d \ln \eta} + (3\gamma - 1)U - 2 = 0. \tag{20}$$

Substituting the definition (19) into the Euler equation (18) and expressing $d \ln P / d \ln \eta$ from (17), we reduce (18) to

$$\frac{dU}{d \ln \eta} = \frac{U(U + 3S - 1)}{1 - U - S}. \tag{21}$$

Substituting (21) into (20), we transform this equation to

$$\frac{dS}{d \ln \eta} = \frac{S[-(2\gamma - 1)U^2 + US + (2\gamma + 1)U + 2S - 2]}{(1 - U)(1 - U - S)}. \tag{22}$$

The original system of three equations (16)–(18) has been thereby reduced to two equations (21), (22), in the same way as it is done for the Sedov–Taylor–von Neumann blast-wave problem [8,9] or Guderley shock-wave implosion [10,11,23]. Once the equations (21), (22) for $U(\eta)$ and $S(\eta)$ have been solved, the self-similar density and pressure profiles, $N(\eta)$ and $P(\eta)$, are immediately found from the mass conservation and adiabaticity integrals

$$N = N_0 \left[S(1 - U)\eta^2\right]^{\frac{1}{\gamma - 1}}, \tag{23}$$

$$P = \frac{1}{\gamma} N_0 \left[S(1 - U)\eta^2\right]^{\frac{\gamma}{\gamma - 1}} = \frac{1}{\gamma N_0^{\gamma - 1}} \cdot N^{\gamma}, \tag{24}$$

respectively (here, N_0 is a positive integration constant). The integral (23) is easily derived from Eqs. (16) and (20). From (23) and (19), we obtain (24). From (23)–(24), we find that the entropy per gas particle,

$$s \propto \ln \frac{p}{\rho^{\gamma}} = \ln \frac{P(\eta)}{[N(\eta)]^{\gamma}} + \mathrm{const} = \mathrm{const}(\eta), \tag{25}$$

is independent of the self-similar coordinate. In other words, the entropy is not only time-independent in each gas particle, which is ensured by our ideal-gas equations, but it is uniform over any part of the flow that does not cross a shock front, which our solutions include at $t > 0$. Post-shock entropy is a constant, too, implying that the shock strength is time-independent.

Equations (21), (22) constituting an autonomous dynamical system (their right-hand sides do not include the independent variable, $\ln \eta$, explicitly) can be analyzed and solved directly, as done in Refs. [8–11] and many others. However, their right-hand sides become singular when either $U = 1$ or $U + S = 1$. The physical origin of these singularities is easy to explain. Note that the gas velocity equals $\eta U(\eta) v_s \, \mathrm{sgn}(t)$, whereas the velocity of the spherical surface $\eta = \mathrm{const}$ equals $\eta v_s \, \mathrm{sgn}(t)$, see Eqs. (12), (13). Therefore, the relative velocity of the surface $\eta = \mathrm{const}$ with respect to the gas particles equals

$$u_\eta = \eta (1 - U) v_s \, \mathrm{sgn}(t). \tag{26}$$

The ratio of this velocity to the local speed of sound, $c_s = \sqrt{\gamma p / \rho} = \eta v_s \sqrt{\gamma P / N}$ defines the local Mach number:

$$M_\eta^2 = \frac{u_\eta^2}{c_s^2} = \frac{1 - U}{S}, \tag{27}$$

see Eqs. (19) and (26). The singularities in the right-hand sides of Eqs. (21), (22) emerge when the velocity of the "constant phase" surface $\eta = \mathrm{const}$ equals one of the characteristic hydrodynamic velocities, either the particle velocity, if $U = 1$, or the speed of sound, if $U + S = 1$. It is convenient to get rid of these singularities through the introduction of an auxiliary dimensionless independent variable τ defined by the equation

$$\frac{d \ln \eta}{d \tau} = (1 - U)(1 - U - S). \tag{28}$$

With the aid of (28), we transform Eqs. (21), (22) into a non-singular autonomous dynamical system

$$\frac{dU}{d\tau} = U(1 - U)(U + 3S - 1), \tag{29}$$

$$\frac{dS}{d\tau} = S \left[-(2\gamma - 1)U^2 + US + (2\gamma + 1)U + 2S - 2 \right], \tag{30}$$

whose trajectories can be qualitatively analyzed using the well-known phase-plane technique [29]. The self-similar profiles $U(\eta)$ and $S(\eta)$ sought for are determined parametrically from the numerical solutions of Eqs. (28)–(30) that yield U, S, and η as functions of τ.

2.3. Phase plane analysis

Equations (29), (30) with the initial and boundary conditions corresponding to (4)–(7) have a one-parameter family of self-similar solutions, the parameter being the Mach number (8) varying in the range $0 < M_0 \leq \infty$. The solutions valid for any $t > 0$ are represented by the trajectories of the dynamical system (29), (30) that approach its singular points at $\tau \to \pm \infty$. It is easy enough to integrate the ordinary differential equations (29) and (30) numerically. To perform such a numerical integration accurately, we have to make sure that the numerical trajectories match the asymptotic solutions of the governing equations near the singular points. For this purpose, we need to understand the phase portrait of the autonomous dynamical system (29), (30), same as when the Guderley problem is solved [10,11,23]. The phase portrait shown in Fig. 2 is equivalent to those schematically presented in Fig. 48 of Ref. [9] and in Fig. 2 of Ref. [22] but plotted in different variables. The arrows show the direction of the increasing radial coordinate η. Below and above the straight line $U + S = 1$ labeled "Sonic line" in Fig. 2, this direction is, respectively, the same or opposite to the direction of the increasing parameter τ.

Physically meaningful solutions of our initial/boundary value problem (1)–(7) are represented on the phase plane (U, S) by the trajectories of the dynamical system (29), (30) that at $\tau \to \pm \infty$ asymptotically approach one of its singular points. These are the points where the right-hand sides of Eqs. (29) and (30) vanish. In Fig. 2 they are labeled P_0, P_1, P_2, P_3, and P_4. Indeed, we describe the gas motion between the center, $r = 0$, and the infinity, $r \to \infty$, as in the situations illustrated with Figs. 1(b), (c), (f), (i), or between a finite value of $r = r_f$ corresponding to the free surface and infinity, as in Figs. 1(e), (g), (h). The center is represented by the singular point P_1 asymptotically approached at $\tau \to -\infty$ if the pressure at the center is zero, and by the singular point at infinity, P_4, approached at $\tau \to +\infty$ if the pressure there is finite. The free surface shown in Figs. 1(e), (g), (h) is represented by the singular point P_3 approached at $\tau \to -\infty$. The sonic wave front shown in Figs. 1(f), (i) is represented by the singular point P_2 approached at $\tau \to -\infty$. Finally, the infinity in all cases is represented by the singular point P_0 approached at $\tau \to +\infty$.

Note that the physically meaningful trajectories cannot cross the straight lines $U = 1$ and $U + S = 1$ where the right-hand side of (28) changes sign. Such a crossing would make the solution multi-valued, which is obviously unphysical. An exception is possible when the crossing occurs at a singular point of the autonomous dynamical system (29), (30), which is the case for the Guderley's converging shock solution [10,11,23], but it does not take place in our case. A phase point representing
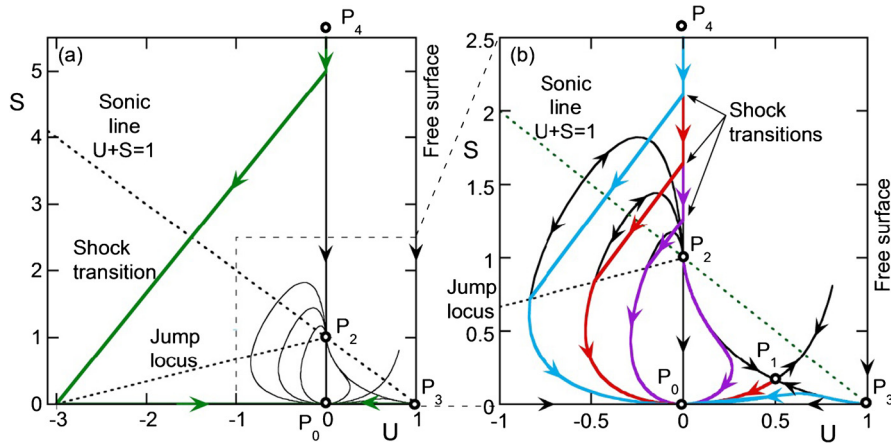
Fig. 2. The phase plane of the dynamical system (29)–(30) for $\gamma = 5/3$. Arrows indicate the direction of increasing radial coordinate η. (a) Thick straight line trajectory segments comprise the classic Noh solution; thin curves correspond to the generalized solutions. (b) A zoomed fragment of (a) marked by dashed lines shows the trajectories that correspond to the generalized Noh solutions in greater detail.

the state of the gas can jump over the sonic line $U + S = 1$ from one phase trajectory to another via a shock front, as demonstrated below.

By the definition (12), the shock front corresponds to a constant value $\eta = 1$ of the self-similar coordinate. It follows from (27) that the Mach numbers of the pre-shock and post-shock flows, indicated by the subscripts 1 and 2, respectively, are given by

$$M_1^2 = \frac{1 - U_1}{S_1}, \qquad M_2^2 = \frac{1 - U_2}{S_2}. \tag{31}$$

The shock density compression for arbitrary shock strength can be expressed via either upstream or downstream Mach number [3] as

$$\frac{N_2}{N_1} = \frac{1 - U_1}{1 - U_2} = \frac{(\gamma + 1)M_1^2}{(\gamma - 1)M_1^2 + 2} = \frac{(\gamma - 1)M_2^2 + 2}{(\gamma + 1)M_2^2}. \tag{32}$$

The post-shock parameters (U_2, S_2) are thereby expressed via the pre-shock parameters (U_1, S_1) as

$$U_2 = \frac{\gamma - 1}{\gamma + 1}U_1 + \frac{2}{\gamma + 1}(1 - S_1), \tag{33}$$

$$S_2 = \frac{2\gamma}{\gamma + 1}(1 - U_1) - \frac{\gamma - 1}{\gamma + 1}S_1. \tag{34}$$

Similarly, one can express (U_1, S_1) via (U_2, S_2) either by solving (33)–(34) or simply making the subscript substitution $1 \leftrightarrow 2$ in Eqs. (33), (34). From (33)–(34) we also find:

$$\frac{S_2 - S_1}{U_2 - U_1} = \gamma, \tag{35}$$

i.e., the slope of the straight line segment representing a shock transition on the (U, S) phase plane does not depend on the shock strength and equals γ.

Fig. 2 and an inspection of Eqs. (29), (30) show that the straight lines $U = 0$, $U = 1$, and $S = 0$ are invariant: segments of these lines connecting singular points are trajectories of the system. Physically, they represent a uniform resting gas, a free surface of the gas, and an adiabatic motion of a zero-pressure gas, respectively.

The system (29), (30) has four singular points in the finite part of the phase plane. The point P_0 ($U = 0, S = 0$) is a node attracting at $\tau \to +\infty$. All the solutions satisfying both the initial conditions (4)–(6) and the boundary conditions (7) at $r \to \infty$ are represented on the phase plane by the trajectories approaching P_0 at $\tau \to +\infty$, which corresponds to $\eta \to \infty$. Indeed, Eq. (12) shows that in the limit $t \to 0$, the self-similar coordinate η corresponding to any finite value of the radial coordinate r tends to infinity. Asymptotic solutions of Eqs. (21), (22) in the vicinity of the singular point P_0 are $U \cong \text{const}_1 \cdot \eta^{-1}$, $S \cong \text{const}_2 \cdot \eta^{-2}$ at $\eta \to \infty$, where const_2 cannot be negative and const_1 can have either sign. Equations (13), (23), (24) demonstrate that in this limit, the gas velocity, density, and pressure tend to constant values, which is consistent with (4)–(7) and Figs. 1(a), (d). This observation explains why only the part of the phase plane containing the trajectories approaching P_0 in the limit $\tau \to +\infty$ from above, that is ($U \leq 1, S \geq 0$), is of interest here.

The saddle point $P_1(U = \frac{2}{3\gamma - 1}, S = \frac{\gamma - 1}{3\gamma - 1})$ represents the state of the gas at the center, $r = 0$, from which an isentropic rarefaction wave is propagating, or to which an isentropic compression wave is converging. When this saddle points is approached along the separatrix at $\tau \to -\infty$, $\eta \to 0$, we find from Eqs. (19), (23), (24) that the pressure and the density are zero at the center but finite in its vicinity.

The degenerate node $P_2(U = 0, S = 1)$ attracts at $\tau \to -\infty$. From (28) we find that in this limit $\eta \to$ const, so it corresponds to a finite value of the radial coordinate. According to (28), the Mach number describing the motion of this surface $\eta =$ const with respect to the gas particles is unity, which means that this surface is a sonic wave front. It can be the trailing edge of an expanding rarefaction wave, or the front of a converging finite-strength isentropic compression wave, in either case labeled "Sonic wave front" in Figs. 1(f) and (i). This front either leaves behind, as in Fig. 1(f), or propagates into, as in Fig. 1(i), a uniform resting finite-pressure gas core near the center. In either case, it propagates at the speed of sound characteristic of the core.

The degenerate node $P_3(U = 1, S = 0)$ attracts at $\tau \to -\infty$. Similarly, from (28), we find that in this limit $\eta \to$ const, so it corresponds to a finite value of the radial coordinate. From (19), (23), and (24) we conclude that both the pressure and density of the gas vanish in this limit, implying that this singular point corresponds to a boundary between the gas and the vacuum, which is labeled "Free surface" in Figs. 1(e), (g), (h). This free surface can either be the outer boundary of a vacuum cavity left behind an expanding rarefaction wave, as in Fig. 1(e), or the inner boundary of a collapsing cavity, as in Figs. 1(g), (h).

In addition, there is an important singular point at infinity, the saddle point $P_4(U = 1, S \to +\infty)$, where the right-hand side of Eq. (29) vanishes but the right-hand side of Eq. (30) does not. It represents a finite-pressure gas at the center, $\eta = 0$. The semi-infinite ray of the invariant straight line $U = 0$ connecting the singular points P_4 and P_2 represents the "Uniform gas core at rest" in Figs. 1(f), (i). Indeed, after substituting $U = 0$ into Eq. (22), we immediately integrate it to obtain $S =$ const $\cdot \eta^{-2}$, where the integration constant must be positive. Substituting this expression into Eqs. (23), (24), we find that both the pressure and the density are constant along this segment. A finite segment of this ray represents the "Uniform shocked gas at rest" in Figs. 1(b), (c), that is, the locus of post-shock states on our phase plane. To find the locus of the corresponding pre-shock states, we note that a shock front is represented with a jump from one trajectory to another, with the pre-and post-shock values of U and S satisfying the Hugoniot conditions (33), (34). Substituting $U_2 = 0$ into (33), we determine the locus sought for, which also turns out to be a straight-line segment:

$$S_1 = 1 + \frac{\gamma - 1}{2} U_1, \tag{36}$$

where

$$-\frac{2}{\gamma - 1} \leq U_1 < 0. \tag{37}$$

In Fig. 2, the segment (36) is shown as a dotted line labeled "Jump locus." The range (37) of U_1 is bounded from below by the requirement that the pre-shock value of $S_1 \geq 0$; here, the equality corresponds to a strong expanding shock. The interval (37) is bounded from above by the requirement that the Mach number of the shock front $M_1 > 1$; as the parameter U_1 approaches zero, the weak-shock front reduces to a sonic front. The jumps from the "Jump locus" segment to the post-shock locus segment are shown in Fig. 2 as straight-line segments labeled "Shock transitions" with arrow indicating the direction of increase of the radial coordinate η. The relation (35) explains why all these segments in Fig. 2(b) are parallel to each other.

2.4. Solutions

2.4.1. The classic Noh solution

The classic Noh solution is typically considered at $t > 0$. However, it can be analytically continued to negative time, being a branch of a solution valid at $-\infty < t < +\infty$, see Figs. 1(b) and (g). The same can be said about the Guderley shock-wave implosion problem but not about the Sedov–Taylor–von Neumann blast-wave problem. Here, we start with the implosion phase $t < 0$, when a cavity in a cold gas collapses onto the center at a constant velocity, as in Fig. 1(g). We describe the self-similar solution for the converging flow. On the phase plane, this solution is represented by a segment of the invariant straight line $S = 0$ connecting the singular points P_3 and P_0. Substituting $S = 0$ into (21), we immediately obtain

$$U = \frac{U_\infty}{\eta}, \tag{38}$$

where U_∞ is a positive integration constant to be determined. The solution (38) means that the gas velocity profile is flat, as should occur in the absence of a pressure gradient. To obtain the density profile, we cannot use the integral (23) because S vanishes. Instead, we integrate the continuity equation (16) together with (38) to obtain

$$N = \begin{cases} (1 - \frac{U_\infty}{\eta})^2, & \eta \geq U_\infty; \\ 0, & 0 < \eta < U_\infty. \end{cases} \tag{39}$$

The integration constant in (39) is chosen to satisfy the initial condition (5): since at $t \to 0^-$ we have $\eta \to \infty$ for any r, the density profile should satisfy the boundary condition

$$N(\eta \to \infty) = 1. \tag{40}$$

The solution (38)–(39) describes a cavity in a zero-pressure gas collapsing at a constant velocity $U_\infty v_s$ onto the center of symmetry, Fig. 1(g). With negative t approaching $t = 0^-$, the density gradient near the gas–vacuum boundary steepens due to convergence, reproducing at $t = 0^-$ the flat profile (4) shown in Fig. 1(a). The same solution considered at $t > 0$ describes an expansion of a zero-pressure gas from the center, leaving a vacuum behind, which corresponds to a positive sign in front of v_0 in (4). It is similar to that illustrated with Fig. 1(e) but in this case the expansion velocity equals v_0 everywhere, just as the compression velocity in Fig. 1(g).

Now we describe the flow at $t > 0$, after the shock reflection from the center, illustrated with Fig. 1(b). It is represented by a segment of the invariant straight line $S = 0$ entering the singular point P_0 at $\tau \to +\infty$. The density profile in front of the expanding shock must be given by same solution (39) with the substitution $U_\infty \to -U_\infty$ because at $t > 0$ the pre-shock mass converging at a constant velocity has a negative self-similar velocity U. Then the pre-shock velocity and density profiles are, respectively,

$$U = -\frac{U_\infty}{\eta}, \tag{41}$$

$$N = \left(1 + \frac{U_\infty}{\eta}\right)^2, \quad \eta > 1. \tag{42}$$

In the resting shocked gas $U = 0$, and the integration of Eq. (22) results in

$$S = \frac{S_0}{\eta^2}, \quad \eta \leq 1, \tag{43}$$

where S_0 is a positive integration constant to be determined. Equations (23), (24) confirm that the density and pressure profiles behind the shock front are flat, as should occur. To link the pre- and post-shock branches of the solution, we find the intersection of the invariant straight line $S = 0$ representing the pre-shock flow of the converging gas with the "Jump locus" segment (36). It occurs at the left boundary of this segment, where

$$U_1 = -U_\infty = -\frac{2}{\gamma - 1}, \tag{44}$$

and $S = S_1 = 0$. Substituting these values of U_1 and S_1 into the Hugoniot jump conditions (33), (34), we find the post-shock parameters: $U_2 = 0$ and

$$S_2 = S_0 = \frac{2\gamma}{\gamma - 1}. \tag{45}$$

This jump is shown in Fig. 2(a) as the straight line segment labeled "Shock transition." The segment of the straight line $U = 0$ connecting the point $(U = 0, S = S_2)$ with the singular point P_2 represents the locus of the post-shock states on the phase plane. From (4), (44), and (45) we find that the initial dimensional inward velocity of the converging gas is $2v_s/(\gamma - 1) = v_0$, hence

$$v_s = \frac{\gamma - 1}{2} v_0. \tag{46}$$

Using (19), (42), (44), and (45), we find the dimensionless pre- and post-shock densities and the post-shock pressure:

$$N_1 = \left(\frac{\gamma + 1}{\gamma - 1}\right)^2, \qquad N_2 = \left(\frac{\gamma + 1}{\gamma - 1}\right)^3, \qquad P_2 = \frac{2}{\gamma - 1}\left(\frac{\gamma + 1}{\gamma - 1}\right)^3. \tag{47}$$

This concludes the re-derivation of the classic Noh solution, which on the phase plane of Fig. 2(a) is represented by two straight-line trajectory segments and a shock transition across the sonic line, connecting the singular points P_4 (the center, $r = 0$) and P_0 (the infinity, $r \to \infty$). The corresponding velocity, density, and pressure profiles for $\gamma = 5/3$ shown in Fig. 3 are labeled with $M_0 = \infty$. The vertical dotted straight line in the velocity profile indicates the coordinate $\eta = \eta_f = 2/(\gamma - 1)$ of the inner free surface of the converging cold-gas shell; there is no mass at $\eta < \eta_f$, hence, the gas velocity is not defined there.
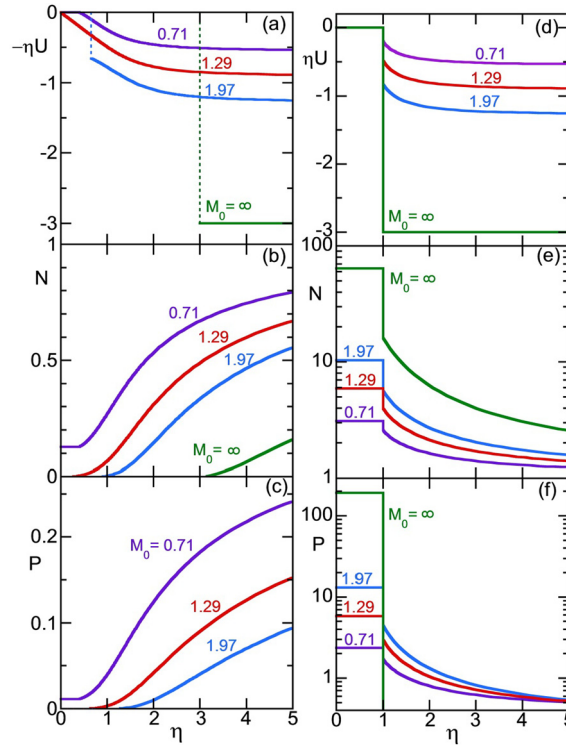
Fig. 3. Self-similar velocity, density, and pressure profiles for the classic Noh solution ($M_0 = \infty$) and generalized Noh solutions with finite $M_0 = 0.710148$ to 1.97201, at $\gamma = 5/3$. The profiles on the left, (a) to (c), correspond to the implosion phase of the motion, $t < 0$, and the profiles on the right, (d) to (f) – to the stagnation via an expanding accretion shock wave phase, $t > 0$.

2.4.2. Collapse of a cavity in a finite-pressure gas

We begin with the simplest generalization of the classic Noh solution, for which the implosion phase $t < 0$ describes a finite-pressure gas collapsing at a constant velocity onto a vacuum cavity, as schematically shown in Fig. 1(h). At $t = 0^-$, the gas reaches the center, and the initial conditions (4)–(6) are satisfied. In the phase plane of Fig. 2(b), the trajectories corresponding to the solutions of this type fill a curvilinear triangle formed by the separatrices linking the singular points P_1 and P_0, P_3 and P_1, and the segment of the straight line $S = 0$ connecting P_3 with P_0. The implosion phase is described by any trajectory connecting the singular points P_3 (free surface) and P_0 (infinity) outside of the straight line $S = 0$ that represents the cold-gas collapsing-cavity solution given in Section 2.4.1. There is a one-parameter family of such solutions defined by $M_{0,\mathrm{cr}} < M_0 < \infty$, where the critical Mach number value for $\gamma = 5/3$ equals 1.28861, as explained below. Here, we present an example of such solution that on the phase plane (U, S) corresponds to the curvilinear trajectory of this type shown in Fig. 2(b).

Equations (28)–(30) are numerically solved using the Rosenbrock integration method [30] as appropriate for stiff differential equations. The numerical integration can be started from any non-singular point in this domain, $U = U_m$, $S = S_m$, assuming additionally $\eta_m = 1$ (later we will have to re-scale the self-similar radial coordinate). The first step is the integration of (28)–(30) from this point to a large negative τ, approaching the singular point P_3, although not reaching it. It can be shown that all the trajectories outside of the invariant lines $U = 1$ and $S = 0$ approach the degenerate node P_3 at $\tau \to -\infty$ with the same slope. Asymptotically, at $\theta = \ln(\eta/\eta_f) << 1$, we have

$$U = 1 - \frac{3(\gamma - 1)}{\gamma + 1}\theta + \frac{3(\gamma - 1)(9\gamma^2 - 20\gamma + 7)}{2(\gamma + 1)^2(3\gamma - 5)}\theta^2 + O\left(\theta^3\right);$$
$$S = \frac{(2 - \gamma)(\gamma - 1)}{\gamma + 1}\theta - \frac{(2 - \gamma)(\gamma - 1)(13\gamma^2 - 20\gamma + 3)}{2(\gamma + 1)^2(3\gamma - 5)}\theta^2 + O\left(\theta^3\right).$$

(48)

The second- and higher-order terms in the expansions (48) diverge at $\gamma = 5/3$. For this special case, we have instead

$$U = 1 - \frac{3}{4}\theta + \frac{9}{32}\theta^2 \ln\theta + O\left(\theta^2\right); \qquad S = \frac{1}{12}\theta - \frac{13}{96}\theta^2 \ln\theta + O\left(\theta^2\right).$$

(49)

One can use (48) or (49) to analytically extrapolate the solution from the farthest point reached with the numerical integration to the actual position of the free surface where the gas pressure and density vanish, which corresponds to a
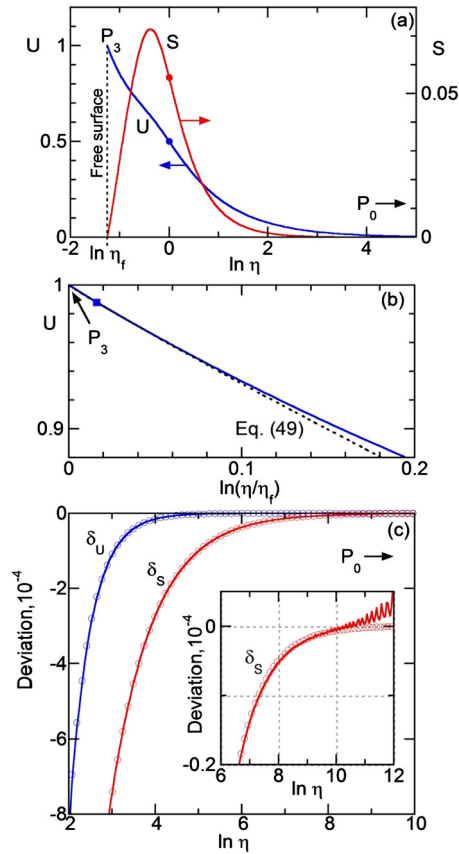
Fig. 4. (a) Profiles of U and S obtained for $\gamma = 5/3$ and $M_0 = 1.97201$. The corresponding solutions describe a collapse of a cavity in a finite-pressure gas at $t < 0$ and an expansion of a rarefaction wave leaving vacuum behind at $t > 0$. The filled circles mark the starting point of numerical integration, the dotted line indicates the position of the free surface that corresponds to the singular point P_3 on the phase plane. (b) The numerical profile of the self-similar velocity U (solid line) and the asymptotic solution (dotted line labeled Eq. (49)) in the vicinity of the free surface. (c) Deviations (53) of the numerical profiles of ηU and $\eta^2 S$ from the asymptotic values, U_∞ and S_∞, respectively, shown in units of 10^{-4}: numerical solutions (lines) vs. Eqs. (51), (52) (symbols). Insert: the same δ_S curve zoomed at large values of $\ln \eta$ shows how the numerical noise starts contaminating the solution.

certain finite value of the radial coordinate $\eta = \eta_f$ indicating the boundary of the empty cavity. Near this boundary, the velocity approaches the finite value $v_s \eta_f$, whereas the density and pressure vanish as

$$N \propto (\eta - \eta_f)^{\frac{2}{\gamma-1}}, \qquad P \propto (\eta - \eta_f)^{\frac{2\gamma}{\gamma-1}}, \tag{50}$$

respectively. These formulas are easily obtained by substituting the asymptotic expressions (48), (49) into the integrals (23), (24).

Fig. 4(a) presents the results of numerical integration obtained for $\gamma = 5/3$ with $U_m = 1/2$ and $S_m = 1/12$. Solid circles mark the starting point of the integration where we have assumed $\ln \eta = 0$. The left boundary of the profiles, $\eta = \eta_f$, corresponds to the free surface represented by the singular point P_3 in the phase plane. Far to the right, at $\eta \to \infty$, the trajectory asymptotically approaches the singular point P_0. Fig. 4(b) shows the profile of U in the vicinity of the free surface. The solid box indicates the location where the numerical simulation ended. Beyond this point, the profiles were extrapolated with the aid of (49) to the position of the free surface, which in this case is $\ln \eta_f = -1.25126$. The dotted line labeled "Eq. (49)" in Fig. 4(b) demonstrates the accuracy of the asymptotic approximation (49).

Now we continue with the second step, integrating Eqs. (28)–(30) from the non-singular starting point defined above to a large positive τ, approaching the node P_0. The asymptotic form of the solution in the limit $\eta \to \infty$ is

$$U(\eta) = \frac{U_\infty}{\eta} \left[1 - \frac{1}{\eta^2} S_\infty + O\left(\frac{1}{\eta^3}\right) \right], \tag{51}$$

$$S(\eta) = \frac{S_\infty}{\eta^2} \left[1 - \frac{2\gamma - 3}{\eta} U_\infty + \frac{(2\gamma - 3)(\gamma - 2)}{\eta^2} U_\infty^2 + O\left(\frac{1}{\eta^3}\right) \right], \tag{52}$$

where U_∞ and S_∞ are integration constants evaluated from fitting the results of numerical integration to the asymptotic formulas (51), (52). The fitting procedure is illustrated with Fig. 4(c), where the deviations of the numerical integration results from the first-order asymptotic expressions,

$$\delta_U = \eta U - U_\infty, \qquad \delta_S = \eta^2 S - S_\infty, \tag{53}$$

are plotted in units of 10^{-4} vs. η on a logarithmic scale. Here, the lines show the numerical results, and the symbols are plotted with the aid of Eqs. (51), (52). The comparison illustrates the accuracy of the asymptotic formulas over a wide range of large values of η. The insert is a zoomed fragment of the same graph for $\ln \eta$ ranging from 6 to 12. We see that at $\ln \eta > 10$, when U and S become less than 10^{-4} and 10^{-9}, respectively, the solution becomes increasingly contaminated by the numerical noise. This is why, in order to control the numerical accuracy of determination of the parameters U_∞ and S_∞ one has to compare the results of numerical integration with the asymptotic formulas over a wide range of η.

From (12)–(15), and (19), we find that the gas velocity and the local speed of sound at $\eta \to \infty$ tend to $v_s U_\infty$ and $v_s \sqrt{S_\infty}$, respectively. Therefore, the Mach number (8) is expressed via these constants as

$$M_0 = \frac{|U_\infty|}{\sqrt{S_\infty}}. \tag{54}$$

Note that construction of the solution described above leaves the scale of the radial coordinate η, and hence, the values of U_∞ and S_∞, arbitrary. The coordinate η enters Eq. (28) only via $d \ln \eta$, which means that our equations and the asymptotic formulas (51), (52) are invariant under a scale symmetry transformation

$$\eta \to \lambda \eta, \qquad U_\infty \to \lambda U_\infty, \qquad S_\infty \to \lambda^2 S_\infty, \tag{55}$$

where λ is an arbitrary positive scaling factor. The asymptotic formula (54) for the Mach number is also invariant under the transformation (55).

We remove this arbitrariness in the scale of η by requiring that the expanding shock front coordinate is $\eta = 1$, as defined by Eq. (12). To do this, we need to construct the solution for the stagnation phase at $t > 0$ schematically shown in Fig. 1(c). For this purpose, we start our numerical integration from the "Jump locus" straight line segment (36), (37). Specifically, we choose an arbitrary negative trial value of $U = U_1$ in the range (37), determine the corresponding positive value of $S = S_1$ from (36), and take the initial value of $\eta = 1$, as appropriate for the shock front position. We integrate Eqs. (28)–(30) from this starting point to a large positive τ, approaching the node P_0. Then we evaluate the constants U_∞ and S_∞ from (51), (52), as explained above, and the corresponding value of M_0 from (54). If the latter is larger or smaller than the above value of M_0 found for the trajectory connecting the singular points P_3 and P_0, then we must chose a different trial value of U_1, closer to the left or right boundary of the interval (37), which correspond to the limits of $M_0 \to \infty$ and $M_0 \to 0$, respectively. With a simple shooting method that rapidly converges, we find the value of U_1 that, within our numerical accuracy, corresponds to the same value of M_0 that we have determined at the previous step, as well as the accurate values of U_∞ and S_∞. From (31), (32) we find the Mach number of the expanding shock wave, and the density and pressure jumps:

$$M_1 = \sqrt{\frac{2(1 - U_1)}{2 + (\gamma - 1)U_1}}, \qquad \frac{N_2}{N_1} = 1 - U_1, \qquad \frac{P_2}{P_1} = \frac{2 - (\gamma + 1)U_1}{2 + (\gamma - 1)U_1}. \tag{56}$$

The analytic continuation of the solution from $t < 0$ to $t > 0$ implies that the corresponding trajectories entering the singular point P_0 at $\tau \to \infty$ from the left and right side are characterized by the same value of S_∞ and the values of U_∞ differing only in sign. Since both branches of the solution yield the same value of M_0, the values of U_∞ and S_∞ from the solution that describes the implosion phase are transformed to the above values by the scaling transformation (55) that yields the appropriate value of the scaling factor λ. The same transformation determines the scale of the coordinate η for the implosion phase of the solution.

Self-similar profiles of the physical variables are constructed using (13)–(15), (23), (24). In particular, the shock velocity is given by $v_s = v_0/|U_\infty|$. The boundary condition (40) implies that in (23), (24) the integration constant equals $N_0 = S_\infty^{-\frac{1}{\gamma-1}}$. The velocity, density and pressure profiles constructed for this case in Fig. 3 are labeled by the corresponding rounded-up value of the Mach number, which in this case is $M_0 = 1.97201$. The vertical dotted straight line in the velocity profile indicates the inner coordinate $\eta = \eta_f = 0.654522$ of the free surface separating the converging gas from the vacuum inside it. Note that during the convergence phase, $t < 0$, the physical velocity (13) equals $v_s \times (-\eta U)$, which for the trajectory connecting the singular points P_3 and P_0 is negative, as shown in Fig. 3. At $t > 0$, the same trajectory corresponds to a solution describing the expansion of a strong rarefaction wave, leaving cavitation behind, as schematically shown in Fig. 1(e). For such solution, the velocity profiles are the same as in Fig. 3 but with a different sign, whereas the density and pressure profiles are exactly the same.

The right part of Fig. 3 shows the profiles plotted for the stagnation phase, $t > 0$. Generally, they are similar to those characteristic of the classic Noh solution, but there is one important difference. Due to a finite pre-shock pressure, the isentropic density increase caused by the convergence of the flow results in a corresponding pressure increase, creating a negative pressure gradient in the radial direction. The pressure gradient, in turn, slows down the incident gas. Hence, the velocity profile is no longer flat, in contrast with the classic case of $M_0 = \infty$. The shock strength is finite, too: for this example, the upstream shock Mach number M_1, the density and pressure jumps in the expanding shock front found from (56) are 1.59423, 1.83454, and 2.92693, respectively.

2.4.3. The intermediate case and the critical value of M_0

The next case we illustrate here corresponds to the intermediate case when, during the implosion phase $t < 0$, the vacuum cavity inside the converging shell shrinks into a point. Therefore, the gas fills the whole space, its density vanishing at the center only. The imploding flow is a finite-strength isentropic compression wave that produces the initial conditions (4) at $t = 0^-$, Fig. 1(a), after which a finite-strength expanding stagnation shock is formed, as in Fig. 1(c). In the phase plane of Fig. 2(b), the intermediate-case solution is represented by the separatrix connecting the saddle point P_1 and the node P_0. As demonstrated by Fig. 2(b), this separatrix separates two qualitatively different types of trajectories: those linking the singular points P_3 and P_0, see Section 2.4.2 above, and those linking the singular points P_2 and P_0, see Section 2.4.4 below. Therefore, the Mach number characteristic of the separatrix linking the singular points P_1 and P_0 represents the critical value of this parameter, $M_0 = M_{0,cr}$. For $\gamma = 5/3$ the critical value equals $M_{0,cr} = 1.28861$, see below. Larger values of $M_0 > M_{0,cr}$ correspond to the solutions described in Sections 2.4.1 and 2.4.2 above and illustrated with Figs. 1(e) and (h). Smaller values of $M_0 < M_{0,cr}$ correspond to the solutions described in Section 2.4.4 below and illustrated with Figs. 1(f) and (i).

Linearization of Eqs. (29)–(30) in the vicinity of the saddle point P_1 yields the eigenvector corresponding to the direction of the separatrix that asymptotically approaches this point at $\tau \to -\infty$ from lower values of U and S. We put the starting point of our numerical integration on the separatrix, as close to the singular point P_1 as our numerical accuracy permits, and extrapolate the separatrix entering the saddle P_1 to $\tau \to -\infty$, $\eta \to 0$ using the linear approximation. Taking the limit $\eta \to 0$ in the integrals (23), (24), we find that the self-similar density and pressure tend to zero near the center following the asymptotic formulas (50) with $\eta_f = 0$, as should occur. Then we integrate (28)–(30) numerically to large positive values of τ, approaching the node P_0, and determine the values of U_∞ and S_∞ from (51), (52). The critical Mach number is evaluated as described in Section 2.4.2. For $\gamma = 5/3$ it equals $M_{0,cr} = 1.28861$. Here again, the symmetry (10) transforms the implosion solution valid at $t < 0$ into a solution that describes the expansion an isentropic spherical rarefaction wave at $t > 0$. The corresponding velocity profiles differ from those shown in the left part of Fig. 3 by the sign only, whereas the density and pressure profiles are exactly the same.

The generalized expanding-shock Noh solution for the stagnation phase, $t > 0$, Fig. 1(c). is found exactly in the same way as in Section 2.4.2. In particular, the upstream shock Mach number M_1, the density and pressure jumps in the expanding shock front found from (56) are 1.32892, 1.48218, and 1.95754, respectively. The velocity, density and pressure profiles constructed for this case in Fig. 3 are labeled by the corresponding rounded-up value of the Mach number M_0.

2.4.4. Convergence of a finite-strength compression wave

Another example of the generalized Noh solution at the implosion phase $t < 0$ corresponds to a finite-strength compression wave spherically converging into a uniform resting gas near the center, Fig. 1(i). In the phase plane of Fig. 2(b), the trajectories corresponding to the solutions of this type fill the curvilinear triangle formed by the separatrices linking the singular points P_1 and P_0, P_2 and P_1, and the segment of the straight line $U = 0$ connecting P_2 with P_0. The implosion phase is described by any trajectory connecting the singular points P_2 and P_0 outside of the invariant straight-line segment ($U = 0$, $0 < S < 1$). There is a one-parameter family of such solutions characterized by $0 < M_0 < M_{0,cr} = 1.28861$, of which we present one example that corresponds to the trajectory of this type shown in Fig. 2(b).

The singular point P_2 is located on the sonic line $U + S = 1$, which means that it physically corresponds to a sonic wave front. Solutions approaching the singular point P_2 at $\tau \to -\infty$ describe the fronts either of finite-strength isentropic compression wave propagating into a uniform gas core at rest, Fig. 1(h), or of a rarefaction wave leaving a uniform gas core at rest behind it [9], Fig. 1(e). Such a front is a weak discontinuity, which means that the density and pressure are continuous at the sonic front but their radial derivatives are not. The numerical solution is constructed in the same way as above. We choose an arbitrary non-singular starting point inside the curvilinear triangle (to plot the trajectory shown in Fig. 2(b), we have chosen $U_m = 1/4$ and $S_m = 1/6$) and perform a numerical integration to a large negative τ approaching the degenerate node P_2, and then to a large positive τ approaching P_0.

The generalized expanding-shock Noh solution for the stagnation phase, $t > 0$, Fig. 1(c), is found exactly in the same way as in Sections 2.4.2, 2.4.3. The initial expansion velocity for this case is lower than those found for the above two cases, with $M_0 = 0.71048$, and the expanding shock is weaker. The upstream shock Mach number M_1, the density and pressure jumps in the expanding shock front found from (56) for this case are 1.13090, 1.19556, and 1.34866, respectively. The self-similar profiles calculated for this case are also shown in Fig. 3.

Table 1
Parameters of the self-similar solutions illustrated with Figs. 5–7.

Mach number M_0	0.710148	1.28861	1.97201
Initial velocity v_0, cm/μs	0.916798	1.66359	2.54585
Radius of the free surface at $t = 1$ ns, μm	n/a	0.	13.0622
Radius of the sonic front at $t = 1$ ns, μm	6.49046	0.	n/a
Density behind the sonic front, g/cm^3	0.127073	0.	n/a
Accretion shock Mach number M_1	1.13090	1.32892	1.59423
Accretion shock velocity, cm/μs	1.67763	1.83409	1.99569
Radius of the shock front at $t = 3$ ns, μm	16.7763	18.3409	19.9569
Pre-shock density, g/cm^3	2.59276	3.97829	5.62914
Post-shock density, g/cm^3	3.09980	5.89655	10.3269
Pre-shock pressure, Mbar	4.89332	9.98837	17.8130
Post-shock pressure, Mbar	6.59943	19.5526	52.1377

3. Numerical simulations

3.1. Three specific verification tests and sample numerical simulations

In this subsection we propose three specific verification tests that span qualitatively different regimes in Mach number space described in Section 2.4. Each of these three tests is designed to examine, in a single simulation, a sequence of all three different phases within that specific Mach number regime: isentropic expansion, isentropic compression, and stagnation via an accretion shock wave.

The first phase, isentropic expansion, begins by initializing the simulation with a uniform positive (outward) velocity, as in Fig. 1(d). The symmetry (9) ensures that the exact solutions of our initial/boundary value problem are self-similar, and the simulated solutions of our governing equations (1)–(3) should approximate them. The semi-analytic solutions presented in Section 2 are self-similar exactly, by construction. Of course, their evaluation involves the use of numerical integrators of the ordinary differential equations (28)–(30) and of the asymptotic formulas, such as (48), (49), (51), and (52), hence, the evaluated solutions are approximate, not exact. But their accuracy is easily increased by straightforward means to values far exceeding the accuracy that we can expect from solving our governing partial differential equations (1)–(3) on a numerical grid. Therefore the self-similar solutions of Section 2 are, or can be made, as useful for code verification as the exact (i.e. explicit) ones [11].

Having checked our numerical solution during the isentropic expansion phase, we use the symmetries (10), (11) to generate the numerical solutions involving convergence. Specifically, we choose a certain value $t = t_0$, stop the numerical run at $t = t_0/2$, change the sign of all the velocities (10), and make the time translation (11). The numerical solution provides the profiles characteristic of the isentropic expansion at the moment $t = t_0/2$. The symmetries (10), (11) ensure that the same profiles of density and pressure, and the velocity profile with a reversed sign, are characteristic of the corresponding isentropic-compression solution, Figs. 1(h), (i). We thereby produce the second phase of the flow, an isentropic compression back to the initial state, which, after evolving for $t_0/2$ more, should reproduce the Noh initial conditions, same as in Fig. 1(a), but at $t = t_0^-$. At this point, the third and final phase of the flow begins, that of an outwardly-propagating shock wave, analogous to that of the classic Noh problem, but of course generalized in the senses that we have discussed here. For our numerical examples below, we have chosen $t_0 = 2$ ns. The solutions we have developed here apply to all three of these phases, yielding semi-analytic solutions to which numerical simulations can be compared at any time during the evolution of the fluid, subject only to the condition that we ensure that the numerical accuracy of the former far exceeds that of the latter.

The particular code that we use here for comparison purposes (and later for verification purposes) is Cerberus, an internally-developed Eulerian high-order Godunov code. It uses a piecewise-linear reconstruction technique originally developed by Colella and Glaz [31], which in turn was inspired by the MUSCL code of van Leer [32]. Cerberus is described in more detail in [16], where a verification of its MHD version vs. our magnetized Noh solution was demonstrated. The only aspect of Cerberus that may distinguish it from other similar codes in the community is that it does not use an approximate Riemann solver, but rather one that is commonly referred to as "exact," meaning that exact analytic formulae for shocks, rarefactions, and contact discontinuities are used within the solver, and that the resolved state at a particular flux point in computed by iterating until the errors are extremely small. In particular, such "exact" solvers are capable of recognizing true cavitation, and assigning zero fluxes to those interfaces for which cavitation occurs. This may bear on the results to be presented below for the higher Mach number regime.

We perform our simulations as follows. All the simulations are initiated with the aid of the initial conditions (1)–(3). Specifically, we have chosen the dimensional density and pressure scale factors $\rho_0 = 1$ g/cm^3 and $p_0 = 1$ Mbar, and gas $\gamma = 5/3$. The value of the isentropic speed of sound corresponding to our initial conditions is $c_{s0} = 1.29099$ cm/μs. The Mach number values calculated for the examples of Section 2, $M_0 = 0.710148$, 1.28861 and 1.97201 translate into the velocities $v_0 = 0.916798$, 1.66359, and 2.54585 cm/μs, respectively. Table 1 presents the numerical parameters characteristic of the three above solutions.
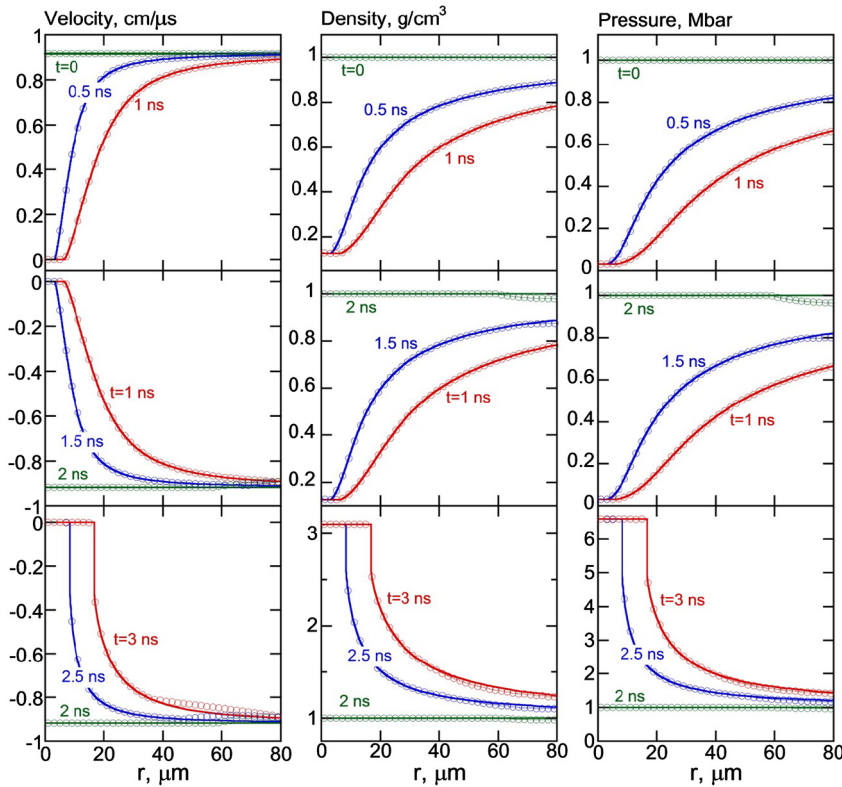
Fig. 5. Analytical (lines) and numerical (symbols) profiles of velocity, density, and pressure for $M_0 = 0.710148$.

All our simulations are initiated at $t = 0$, with the plus sign in front of v_0 in (1). They describe isentropic finite-strength expansion waves that are predicted to leave behind a uniform resting gas for $M_0 = 0.710148$ or a vacuum cavity for $M_0 = 1.97201$. Each simulation is run from $t = 0$ to $t = 1$ ns, forming the velocity, density, and pressure profiles characteristic of the corresponding expansion waves. The isentropic flows of an ideal fluid are reversible, permitting the symmetry transformation $t \to -t$, $v \to -v$. We restart our simulation at $t = 1$ ns, using as the initial conditions the numerically generated profiles of density and pressure, at the same time reversing the sign of the numerical velocity profile. Ideally, at any intermediate time, say, $t = 1.5$ ns, the simulation should reproduce the profiles of density and pressure previously generated at the corresponding moment of the expansion, in this case for $t = 0.5$ ns. At $t = 2$ ns, we should reproduce the initial conditions (1)–(3), the flat profiles of all variables, with the negative sign in front of v_0 in (1). After $t = 2$ ns, the simulation should reproduce the self-similar solutions that describe stagnation. Note that the above formulation of the numerical problem does not require the analytical self-similar profiles for the initialization, which is the case, for example, for the Guderley problem [11,12]. Here, the initialization is trivial, as is the velocity reversal. We only need the self-similar profiles generated in Section 2 and shown in Fig. 3 as verification tools, to compare with our Cerberus simulation results.

Such a comparison is presented in Figs. 5, 6, and 7 for $M_0 = 0.710148$, 1.28861 and 1.97201, respectively. The simulations were made on uniform static grid with a grid spacing of 0.1 μm, and a Courant number of 0.5 for all runs. For $M_0 = 0.710148$ and 1.28861 we utilized 800 grid points, which corresponds to the outer boundary of the computational box at $r = 80$ μm. For the case of $M_0 = 1.97201$ the number of grid points was doubled, and the outer boundary was located at $r = 160$ μm. At the outer boundary, we used outflow boundary conditions, i.e., we set the normal derivative of all quantities to zero, which of course is not in agreement with the actual solution, and thus will result in errors which will propagate into the computational domain at the three hydrodynamic characteristic speeds whenever one or more of these speeds is negative.

We see that in all three cases the agreement between our numerical results and the analytic self-similar profiles at the expansion wave phase is quite good. After the velocity reversal at $t = 1$ ns, Figs. 5 and 6 demonstrate a visible difference between the simulation results and the theoretical profiles within a finite distance from the outer boundary, whereas the agreement is still very good closer to the center. The disagreement is due to the zero-gradient boundary conditions at the outer boundary, which do not reproduce the self-similar solution. A sonic wave that starts propagating inward from the outer boundary at the instant of the velocity reversal $t = 1$ ns contaminates the numerical profiles, making them differ from the self-similar ones. For $M_0 = 0.710148$ and 1.28861, the sonic wave reaches $r \approx 50$ and 60 μm, respectively, at $t = 2$ ns. Consequently, the initial conditions (1) are accurately reproduced at $t = 2$ ns only for radii smaller than the above values.
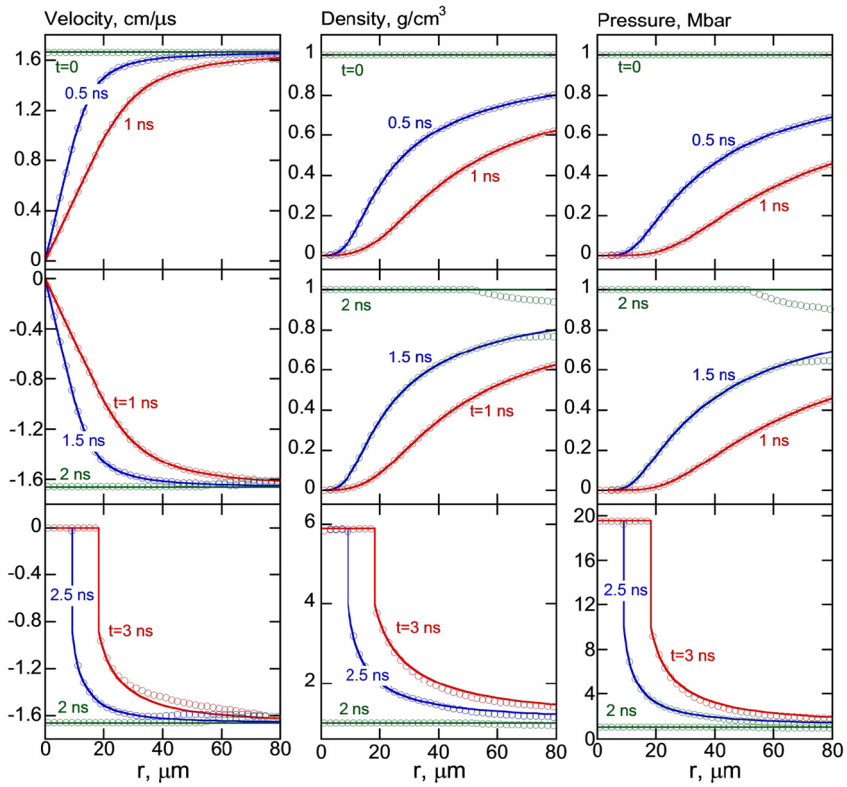
Fig. 6. Analytical (lines) and numerical (symbols) profiles of velocity, density, and pressure for $M_0 = 1.28861$.
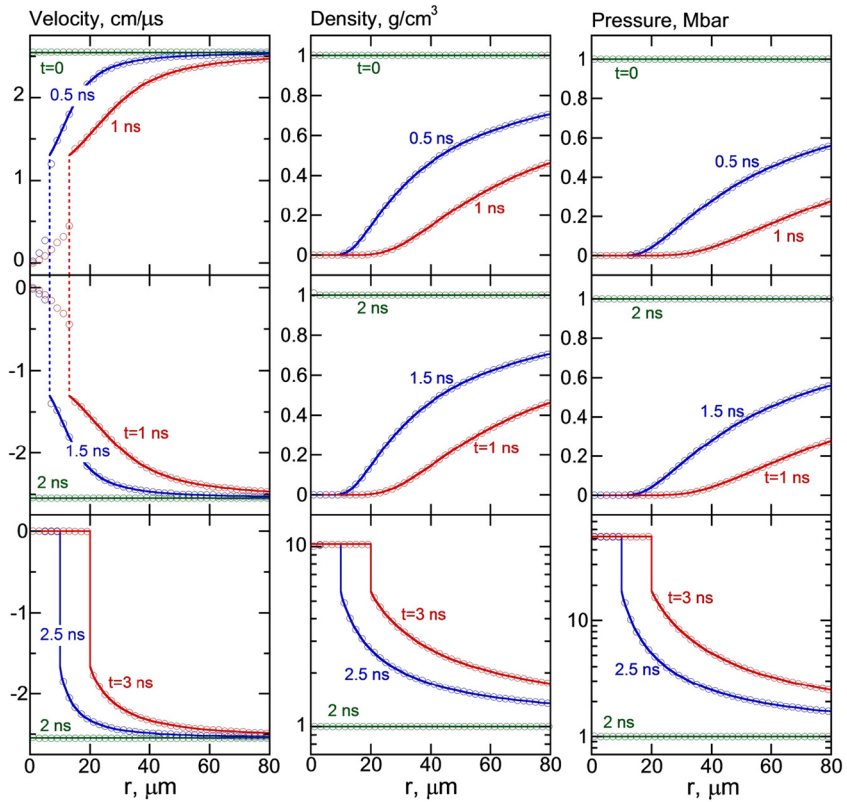

Fig. 7. Analytical (lines) and numerical (symbols) profiles of velocity, density, and pressure for $M_0 = 1.97201$.

This disagreement is not seen in Fig. 7 because here the outer boundary is set farther from the center, and the sonic wave propagating from the boundary does not reach $r = 80$ µm before $t = 2$ ns.

During the stagnation phase that starts at $t = 2$ ns, the sonic wave emitted from the boundary $r = 80$ µm at $t = 1$ ns comes closer to the expanding accretion shock front, contaminating the pre-shock profiles for $M_0 = 0.710148$ and 1.28861 at radii greater than 40 and 25 µm, respectively. Still, it does not yet reach the shock front, so its radial position, pre- and post-shock parameters are well reproduced by the simulations for $M_0 = 0.710148$ and 1.28861, see Figs. 5, 6. As for the case of $M_0 = 1.97201$, the sonic wave emitted from the outer boundary $r = 160$ µm at $t = 1$ ns does not reach the plotted range $r \leq 80$ µm before $t = 3$ ns, so the self-similar pre-shock profiles for the stagnation phase are also well reproduced in the simulation.

We must mention one difficulty encountered by Cerberus for the $M_0 = 1.97201$ case, in which true cavitation is encountered over a finite spatial range. Like all finite volume codes that conserve momentum to roundoff, Cerberus computes velocities by dividing a momentum density by a mass density in each cell. In the cavitation region, this entails dividing extremely small momentum densities by extremely small mass densities, yielding potentially wildly varying velocities. These "velocities" are of course meaningless since the true velocity is undefined in this region. To address this issue, we have imposed a numerical minimum mass density for that case, which we took to be 10^{-7} g/cm^3. This has the effect of giving moderately bounded values to the "velocity" within the cavitation region. In Fig. 7 we have drawn vertical dashed lines to denote the right boundary of the cavitation region. Our simulation velocities to the left of that line thus clearly have no physical meaning. Nonetheless, it is quite heartening to note how closely the discontinuities in those velocities delineate the true right boundary of the cavitation region. Again, this may be due to the fact that Cerberus uses an "exact" Riemann solver which can identify true cavitation events.

3.2. Code verification example

In this subsection we will try to give the reader an example of the primary use to which we hope that the solutions given in this paper will be made, that of code verification. While Figs. 5–7 illustrate the probable correctness of the analytical solutions we present here, and that visually good numerical results for these proposed verification tests are possible, they nonetheless do not constitute true code verification. Code verification involves more than merely verifying that a given code result at a particular resolution looks acceptable when plotted against an analytic solution. Rather it involves an investigation of the behavior of the error as the mesh size is reduced toward zero. The code we shall use in the following verification example is the internally written code Cerberus described earlier in Section 3.1.

We clearly have a wide choice of verification test parameters: Mach number, physical variable, and solution evaluation time. The choice will depend on the use to which a given code is to be put. For example, if one were modeling nearly isentropic flows in which physical dissipation mechanisms are small, a good choice might be the 2 ns entropy solution for any of the Mach numbers, for the errors would give a good indication of the numerical dissipation of the code. Our own interest is in the physics of inertial confinement fusion, in which shocks reflecting off the origin compress and heat plasma, and thus we choose to examine the post-shock density field at a time of 3 ns. To avoid any of the numerical issues with cavitation during the expansion phase of the simulation, which we address later, we choose the $M_0 = 0.710148$ case of Section 2.4.4.

Our verification task will not be as easily performed as for the classic Noh problem. Unlike the classic Noh solutions, the present solutions are not given in terms of closed-form expressions, but rather by numerically integrating ordinary differential equations, albeit to arbitrary precision, producing semi-analytic solutions that are given in tabular form at given solution times. The analytic solution at an arbitrary spatial position thus requires tabular interpolation, which in turn requires an extremely fine tabular mesh to ensure that the interpolation errors are orders of magnitude smaller than the errors in any hydrocode output with which the solution is to be compared. Such tables for the three cases described above, calculated with the same numerical accuracy as Table 1, and with a radial increment of 0.01 µm, are provided in the online supplemental material to this article.

For finite volume codes such as Cerberus, a further numerical step is required, since such codes do not output point values of a quantity, but rather cell averages. Thus one must produce analytic cell averages of the required quantities by numerically integrating the interpolated values over the cells used by the hydrocode. Again, we must ensure that the errors in the analytic cell averages are orders of magnitude smaller than those produced by the hydrocode by utilizing an extremely fine tabular mesh. However, in the example given below, such numerical integration is not necessary, since the analytic solution in the domain of interest is a constant. This should permit the reader to verify his or her own code using the example below, without the need for tabular data of any kind, using only the single density value given in Table 1.

We augmented the $M_0 = 0.710148$ case illustrated with Fig. 5, which used a mesh size of $\Delta r = 0.1$ µm, with three additional calculations using mesh sizes of $\Delta r = 0.2$, 0.05, and 0.025 µm. The outer boundary was located at $r = 160$ µm for all cases to ensure that our numerical results are not contaminated by the boundary effects, cf. Figs. 5, 6. We then computed the cell-average density errors at 3.0 ns for all of the post-shock cells less than a certain radius r_{max}. The latter radius should be, on the one hand, not too small, to avoid the error being dominated by the wall heating phenomenon, but on the other hand, not too large, to avoid the numerical errors associated with the modeling of the shock front, which at this time has reached $r = 16.8$ µm. We have chosen $r_{max} = 15$ µm. For the range $0 < r < r_{max}$, the self-similar solution
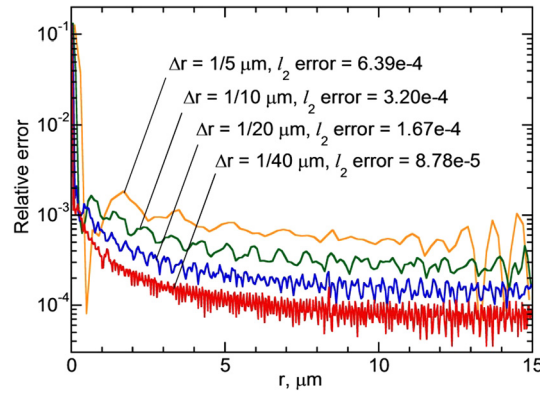
Fig. 8. Profiles of relative errors in the simulated post-shock density for $M_0 = 0.710148$, and the corresponding values of the l_2 error norm (58).

predicts a constant post-shock density $\rho_2 = \rho_0 N_2$, where the value of N_2 is determined from (56), making the calculation of the cell average, and hence the error, trivial. In our particular case, $\rho_2 = 3.09980$ g/cm^3.

The relative values of those errors, $|\bar{\rho}_i/\rho_2 - 1|$, where $\bar{\rho}_i$ is the computed cell-averaged density in the ith cell, are plotted in Fig. 8. Note that the errors are largest in the wall-heated region near the center, and that away from the center the errors monotonically decrease with decreasing grid size, as we had hoped. At the center, note that the maximum error does not change substantially as the grid is refined, but that the radius over which the error is large does monotonically decrease with decreasing grid size. This is consistent with the behavior of high order Godunov codes like Cerberus on the classic Noh problem. For a low resolution, the increase of the numerical error in the vicinity of the shock front is clearly seen, too. Also shown in the plot are the volume-weighted l_2-norms of the error for each of these calculations over this post-shock region, which we denote as simply l_2 error, defined by the general formula

$$l_2 \text{ error} = \frac{1}{\bar{\rho}^a} \sqrt{\sum_{i=1}^{n} (\bar{\rho}_i - \rho_i^a)^2 V_i / \sum_{i=1}^{n} V_i}, \qquad \bar{\rho}^a = \sum_{i=1}^{n} \rho_i^a V_i / \sum_{i=1}^{n} V_i. \tag{57}$$

Here, ρ_i^a is the semi-analytic value of the average density in cell i, V_i is the volume of this cell, and n is the minimum value of i for which the maximum radius of cell i is greater than or equal to r_{max}. In our case, because of our chosen grid sizes, it will always be equal to $r_{max} = 15$ μm, so that $n = r_{max}/\Delta r$. For a spherical geometry, a uniform grid, taking into account that $\rho_i^a = \bar{\rho}^a = \rho_2 = $ const, we reduce Eq. (57) to

$$l_2 \text{ error} = \sqrt{\sum_{i=1}^{n} \left(\frac{\bar{\rho}_i}{\rho_2} - 1\right)^2 \frac{3i^2 - 3i + 1}{n^3}}. \tag{58}$$

As demonstrated by Fig. 8, both the cell-wise errors and the l_2 error norm clearly become smaller as the mesh is refined. Further inspection of the sequence of the l_2 error norms (6.39×10^{-4}, 3.20×10^{-4}, 1.66×10^{-4}, and 8.68×10^{-5}) reveals a convergence rate that is very close to linear. This is the same convergence rate that is typically seen for codes like Cerberus (high-order Godunov codes) on the classic Noh problem, and hence is the convergence rate that we would have anticipated for this problem.

Let us close this section with a mention of the tests that involve true cavitation, in particular the $M_0 = 1.97201$ case which involves cavitation over a finite region, not at just a single point. At the resolution used in Section 3.1, 0.1 μm, we did not encounter any unusual difficulties with that test. Recall that we used an "exact" Riemann solver that recognized true cavitation, but that nonetheless we found it necessary to impose a density floor of 10^{-7} g/cm^3 in order to keep the time step from becoming excessively small. For that resolution, these two attributes proved more than adequate to produce results that looked quite good visually. However, when we tried a convergence series of the kind described for the $M_0 = 0.710148$ case above, the results were quite disconcerting. In particular the wall heating actually became worse as the resolution was increased. We identified this as probably due to some aspect of our treatment of cavitation, since when we initialized the problem with the analytic solution at 2.0 ns, circumventing entirely the cavitation regime and its density floor, these problems vanished. Our conclusion is that while the techniques we used here for dealing with cavitation may appear to work in some cases, we clearly do not have a technique which is applicable to all cases. Treating true cavitation in a hydrodynamic code remains a very difficult problem. It is worth noting that we would have been unaware of this weakness in Cerberus's treatment of cavitation had we not attempted to verify the code using the cavitation solution given here. Clearly, we ourselves have benefited from the use of these solutions as a verification tool. It is our hope that others will also.

4. Conclusions

We have constructed a one-parameter family of self-similar solutions of the compressible Euler equations for hydro code verification. It is parameterized by the Mach number M_0 of the flow at the moment when the profiles of all the flow variables are flat; M_0 can take an arbitrary positive value. Our solutions generalize the classic Noh solution that has been used for verification of practically every code designed to model implosions, explosions, and propagation of shock waves. In our parameterization the classic Noh solution corresponds to the upper limit of our parameter range, $M_0 = \infty$. The other solutions of this family, which correspond to finite positive values of M_0, describe adiabatic compression and expansion of the pre-shock gas and stagnation of this pre-compressed gas in a finite-strength expanding shock wave.

The new solutions are quite similar to the classic ones. The only qualitative difference is that the pre-shock isentropic compression of the converging gas leads to a pressure increase, which, in turn, slows down the converging pre-shock gas. In other words, the pre-shock pressure and velocity profiles shown for these solutions in Figs. 3, 5–7 are no longer flat.

While we have confined ourselves here to an ideal-gas EOS, these one-parameter families of generalized Noh self-similar solutions of the compressible Euler equations can be constructed for an arbitrary EOS of an ideal fluid. In particular, the EOS need not satisfy the Lie symmetry constraints [9,13,14], which must be satisfied in order to construct self-similar solutions of the Sedov–Taylor–von Neumann blast-wave problem [9], and of the Guderley converging-shock problem [10,23]. Formally, this possibility is due to the invariance of both density and pressure under the symmetry transformation (9), which makes self-similar solutions possible for an arbitrary function $p(\rho)$ determining the isentrope. In particular, the EOS does not need to have "normal thermodynamic properties" (as defined in Chapter I, Section 17 of Ref. [20]), which allow the existence of rarefaction fans and compression shocks only. In the vicinity of phase transitions, thermodynamic properties of many materials are "anomalous," making the compression fans and rarefaction shocks possible. The existence of rarefaction shocks had been predicted independently by Bethe [33] and Zel'dovich [34] (see also Chapter I, Section 19 and Chapter XI, Section 20 of Ref. [20]) and confirmed in many experiments [35,36]. Self-similar solutions of the appropriately modified initial/boundary value problem (1)–(7) with a so-called non-convex EOS manifesting the anomalous thermodynamic properties can be obtained in the same way as above. With a non-convex EOS, and a proper choice of parameters, the initial conditions of Figs. 1(a) and (d) can produce at $t > 0$ a self-similar, shockless isentropic stagnation and a self-similar non-isentropic expanding flow with a rarefaction shock wave, respectively.

A common feature of both the classic Noh solution and its generalization discussed here is the uniformity of density and pressure in the resting shocked plasma. This makes it possible to extend the small-amplitude perturbation analysis carried out for the classic Noh case in Ref. [17] to all generalized solutions of this family, including the finite Mach number solutions described here, as well as the non-ideal EOS and/or MHD solutions that can be obtained by the same method. This opens the door to truly multidimensional verification tests, a rarity in the world of compressible hydrodynamics. Specifically, we propose using these perturbed generalized Noh solutions for the verification of two- and three-dimensional hydrodynamics codes, by testing not only the ability of such codes to reproduce the analytic unperturbed one-dimensional solution, but to also to reproduce the proper behavior of small-amplitude perturbations applied to that solution in the transverse directions. In two and three dimensions, the small-amplitude stability analysis should be possible for EOS that displays the D'yakov–Kontorovich (DK) instability [3,37,38] of the accretion shock front. As demonstrated in Refs. [39,40], the presence of the piston driving a planar shock front can qualitatively change the manifestation of this instability. In the generalized Noh problem, the center of symmetry plays the role of the piston. A study of the manifestation of the DK instability in a spherical or cylindrical geometry can uncover interesting physics and lead to the development of advanced code verification tools.

Acknowledgements

Appendix A. Supplementary material

Supplementary material related to this article can be found online at https://doi.org/10.1016/j.jcp.2018.07.054.

References

[1] C.J. Roy, Review of code and solution verification procedures for computational simulation, J. Comput. Phys. 205 (2005) 131–156.
[2] N.E. Kochin, To the theory of discontinuities in fluids, in: Collected Works, vol. 2, Academy of Science of the USSR, Moscow, Leningrad, 1949, pp. 5–42 (in Russian).
[3] L.D. Landau, E.M. Lifshitz, Fluid Mechanics, Pergamon Press, Oxford, New York, 1987.
[4] G.A. Sod, A survey of several finite-difference methods for system of nonlinear hyperbolic conservation laws, J. Comput. Phys. 27 (2005) 1–31.
[5] R. Samtaney, Computational methods for self-similar solutions of the compressible Euler equations, J. Comput. Phys. 132 (1997) 327–345.
[6] W.F. Noh, Errors for calculations of strong shocks using artificial viscosity and an artificial heat flux, J. Comput. Phys. 72 (1987) 78–120.
[7] M. Gehmeyr, B. Cheng, D. Mihalas, Noh's constant-velocity shock problem revisited, Shock Waves 7 (1997) 255–274.
[8] L.I. Sedov, Le mouvement d'air en cas d'une forte explosion, C. R. (Dokl.) Acad. Sci. URSS 52 (1) (1946) 17–20 (in French);
G. Taylor, The formation of a blast wave by a very intense explosion. I. Theoretical discussion, Proc. R. Soc. Lond. Ser. A 201 (1065) (1950) 159–174;
J. von Neumann, The point source solution, in: H.A. Bethe, K. Fuchs, J.O. Hirschfelder, J.L. Magee, R.E. Peierls, J. von Neumann (Eds.), Blast Wave, Los Alamos Scientific Laboratory Report lA-2000, 1958, pp. 27–55 (written in 1947, distributed in 1958).

[9] L.I. Sedov, Similarity and Dimensional Methods in Mechanics, 10th ed., CRC Press, Boca Raton, 1993.

[10] G. Guderley, Starke kugelige und zylindrische Verdichtungsstösse in der Nähe des Kugelmittelpunktes bzw. der Zylinderachse, Luftfahrtforschung 19 (1942) 302–312 (in German).

[11] S.D. Ramsey, J.R. Kamm, J.H. Bolstad, The Guderley problem revisited, Int. J. Comput. Fluid Dyn. 26 (2) (2012) 79–99.

[12] S.D. Ramsey, J.F. Lilienholm, Verification assessment of piston boundary conditions for Lagrangian simulation of the Guderley problem, J. Verif. Valid. Uncertain. Quantificat. 2 (2017) 031001.

[13] S.D. Ramsey, Z.M. Boyd, S.C. Burnett, Solution of the Noh problem using the universal symmetry of the gas dynamics equations, Shock Waves 27 (2017) 477–485.

[14] R.A. Axford, Solutions of the Noh problem for various equations of state using Lie groups, Laser Part. Beams 18 (2000) 93–100.

[15] E.P. Yu, A.L. Velikovich, Y. Maron, Application of one-dimensional stagnation solutions to three-dimensional simulation of compact wire array in absence of radiation, Phys. Plasmas 21 (2014) 082703.

[16] A.L. Velikovich, J.L. Giuliani, S.T. Zalesak, J.W. Thornhill, T.A. Gardiner, Exact self-similar solutions for the magnetized Noh Z pinch problem, Phys. Plasmas 19 (2012) 012707.

[17] A.L. Velikovich, M. Murakami, B.D. Taylor, J.L. Giuliani, S.T. Zalesak, Y. Iwamoto, Stability of stagnation via an expanding accretion shock wave, Phys. Plasmas 23 (2016) 052706.

[18] D.R. Welch, D.V. Rose, C. Thoma, R.E. Clark, C.B. Mostrom, W.A. Stygar, R.J. Leeper, Kinetic simulations of a deuterium–tritium Z pinch with $>10^{16}$ neutron yield, Phys. Plasmas 18 (2011) 056303.

[19] I. Sagert, W.P. Even, T.T. Strother, Two-dimensional implosion simulations with a kinetic particle code, Phys. Rev. E 95 (2017) 053206.

[20] Ya.B. Zel'dovich, Yu.P. Raizer, Physics of Shock Waves and High-Temperature Hydrodynamic Phenomena, 2nd edition, Dover, New York, 2002.

[21] L.V. Ovsiannikov, Group Analysis of Differential Equations, Academic Press, New York, London, 1982.

[22] G. Kagan, X.-Z. Tang, S.C. Hsu, T.J. Awe, Bounce-free spherical hydrodynamic implosion, Phys. Plasmas 18 (2011) 120702.

[23] K.P. Stanyukovich, Unsteady Motion of Continuous Media, Academic Press, New York, 1960.

[24] S. Atzeni, J. Meyer-ter-Vehn, The Physics of Inertial Fusion, Oxford University Press, Oxford, New York, 2004.

[25] R. Lazarus, Self-similar solutions for converging shocks and collapsing cavities, SIAM J. Numer. Anal. 18 (2) (1981) 316–371; Errata, SIAM J. Numer. Anal. 19 (5) (1982) 1090.

[26] R.M. Lock, A.J. Mestel, Annular self-similar solutions in ideal magnetogasdynamics, J. Plasma Phys. 74 (4) (2008) 531–554.

[27] M.A. Liberman, A.L. Velikovich, Self-similar motions in Z-pinch dynamics, Nucl. Fusion 26 (1986) 709–728.

[28] R.C. Wenkatesan, W.H. Choe, Self-similar solutions for the supersonic implosion of a screw-pinch plasma, Phys. Fluids B 4 (1992) 1524–1533.

[29] L.S. Pontryagin, Ordinary Differential Equations, Pergamon Press, London, Paris, 1962, Chapter 2, Section 16.

[30] H.H. Rosenbrock, Some general implicit processes for numerical solution of differential equations, Comput. J. 5 (4) (1963) 329–330;
W.H. Press, S.A. Teukolsky, W.T. Vetterling, B.P. Flannery, Numerical Recipes: The Art of Scientific Computing, 3rd edition, Cambridge University Press, New York, 2007, Section 17.5.1.

[31] P. Colella, H.M. Glaz, Efficient solution algorithms for the Riemann problem for real gases, J. Comput. Phys. 59 (2) (1985) 264–289.

[32] B. van Leer, Towards the ultimate conservative difference scheme. V. A second-order sequel to Godunov's method, J. Comput. Phys. 32 (1) (1979) 101–136.

[33] H.A. Bethe, On the theory of shock waves for an arbitrary equation of state, Report No. 545 for the Office of Scientific Research and Development, Serial No. NDRC-B-237 (May 4, 1942), reprinted in: J.N. Johnson, Roger Chéret (Eds.), Classic Papers in Shock Compression Science, Springer, New York, 1998, pp. 421–495.

[34] Ya.B. Zel'dovich, The possibility of shock rarefaction waves, Zh. Eksp. Teor. Fiz. 16 (4) (1946) 363–364 (in Russian).

[35] A.G. Ivanov, S.A. Novikov, Rarefaction shock waves in iron and steel, Sov. Phys. JETP 13 (6) (1961) 1321–1323.

[36] A.A. Borisov, Al.A. Borisov, S.S. Kutateladze, V.E. Nakoryakov, Rarefaction shock wave near the critical liquid–vapour point, J. Fluid Mech. 126 (1983) 59–73.

[37] S.P. D'yakov, On the stability of shock waves, Zh. Eksp. Teor. Fiz. 27 (3) (1954) 288–295 (in Russian).

[38] V.M. Kontorovich, Concerning the stability of shock waves, Sov. Phys. JETP 6 (6) (1958) 1179–1180.

[39] J.G. Wouchuk, J. López Cavada, Spontaneous acoustic emission of a corrugated shock wave in the presence of a reflecting surface, Phys. Rev. E 70 (4) (2004) 046303.

[40] J.W. Bates, Theory of the corrugation instability of a piston-driven shock wave, Phys. Rev. E 91 (1) (2015) 013014.